



# NURBS functional network approach for automatic image segmentation of macroscopic medical images in melanoma detection

Akemi Gálvez<sup>a,b</sup>, Andrés Iglesias<sup>a,b,\*</sup>, Iztok Fister<sup>b,c</sup>, Iztok Fister Jr.<sup>c</sup>, César Otero<sup>d</sup>, José A. Díaz<sup>d</sup>

<sup>a</sup> Department of Information Science, Faculty of Sciences, Toho University, 2-2-1 Miyama, 274-8510 Funabashi, Japan

<sup>b</sup> Department of Applied Mathematics and Computational Sciences, E.T.S.I. Caminos, Canales y Puertos, University of Cantabria, Avda. de los Castros, s/n, 39005 Santander, Spain

<sup>c</sup> Faculty of Electrical Engineering and Computer Science, University of Maribor, Maribor SI-2000, Slovenia

<sup>d</sup> R&D EgiCAD, School of Civil Engineering, Universidad de Cantabria, Avda. de los Castros 44, 39005 Santander, Cantabria, Spain

## ARTICLE INFO

### Keywords:

Soft computing  
Medical imaging  
Cutaneous melanoma  
Functional networks  
Image segmentation  
Macroscopic images

## ABSTRACT

Image processing techniques are becoming standard technology in many medical specialities, such as dermatology, where they are a key tool for the early detection and diagnosis of melanoma and other skin cancers and tumors. A previous paper by the authors presented at SOCO 2020 conference introduced a new method for image segmentation of skin images through functional networks. The method performs well but it relies on a semi-automatic approach involving a combination of manual and automatic operations. This paper aims at making image segmentation of macroscopic skin images a *fully automatic process*. To this purpose, the present work extends our previous paper with five new relevant contributions: (1) a filtering strategy for removal of noise, hair and other artifacts; (2) two morphological operators for image enhancement; (3) a clustering-based binary classifier to separate the skin tumor from the image background; (4) a smoothing and discretization process to obtain the border points; and (5) a curve reconstruction method from the border points with NURBS using a new type of functional network particularly tailored for this task. This new method is applied to two different benchmarks, comprised respectively of four and two macroscopic medical images of skin tumors. The visual and numerical results show that the method performs very well, yielding segmented images which are suitable for clinical practice. This method is a significant step towards the future development of a fully automatic approach for the whole medical image analysis pipeline of skin images, including diagnosis and classification.

## 1. Introduction

### 1.1. Motivation

One of the most interesting and appealing applications of artificial intelligence (AI) in the fields of medicine and healthcare is the computer-assisted analysis of medical images. AI-powered systems can improve the efficiency of automated image analysis, thus providing valuable support to medical specialists (radiologists, neurologists, cardiologists, neuroscientists, etc.) for the interpretation and diagnosis in non-invasive medical imaging procedures, such as computer tomography (CT), magnetic resonance imaging (MRI), ultrasound images,

positron emission tomography (PET), electro/magnetoencephalography (EEG/MEG), electrocardiography (ECG) and others. Image processing techniques are also widely used in many other medical specialities, such as oncology, surgery, internal medicine, nuclear medicine, and so on.

Among them, dermatology is a medical field where images are pervasive and therefore, computer image analysis plays a fundamental role. Image processing techniques are commonly used nowadays for the analysis of a variety of skin images. They include either *macroscopic images* (obtained through 35 mm standard film cameras, digital cameras, smartphones, tablets and other devices equipped with image sensors) or *microscopic images*, obtained by dermoscopy (also called

\* Corresponding author at: Department of Information Science, Faculty of Sciences, Toho University, 2-2-1 Miyama, 274-8510 Funabashi, Japan.

E-mail addresses: [galveza@unican.es](mailto:galveza@unican.es) (A. Gálvez), [iglesias@unican.es](mailto:iglesias@unican.es) (A. Iglesias), [iztok.fister@um.si](mailto:iztok.fister@um.si) (I. Fister), [iztok.fister1@um.si](mailto:iztok.fister1@um.si) (I. Fister), [cesar.otero@unican.es](mailto:cesar.otero@unican.es) (C. Otero), [joseandres.diaz@unican.es](mailto:joseandres.diaz@unican.es) (J.A. Díaz).

URL: <http://personales.unican.es/iglesias> (A. Iglesias).

<https://doi.org/10.1016/j.jocs.2021.101481>

Received 18 April 2021; Received in revised form 10 September 2021; Accepted 13 October 2021

Available online 3 November 2021

1877-7503/© 2021 Elsevier B.V. All rights reserved.

epiluminescence microscopy) or other photomicrography techniques. Most of this research effort is focused on the early detection, diagnosis and treatment of different types of skin lesions and tumors, mainly skin cancer. The present work is also devoted to this problem.

Skin cancer can be roughly classified into melanoma and non-melanoma skin cancer. In this paper, we will focus on the *melanoma* skin cancer (also called *malignant melanoma* or *cutaneous melanoma*), a type of cancer arising from cells called *melanocytes* that contain a brown pigment called *melanin*, which protects the deeper layers of the skin from some of the harmful effects of the sun and gives the skin its tan or brown color. The cancer starts when such cells begin to grow out of control, at the risk of spreading to nearby lymph nodes, internal organs and other parts of the body. Melanoma is less common than the other types of skin cancer, accounting for only about 1% of skin cancers, but it is the most dangerous one, as it is more likely to grow and spread to other parts of the body. In fact, melanoma causes a large majority of skin cancer deaths. For instance, the World Health Organization reported that in 2015 more than 3.1 million people was affected by melanoma worldwide, with about 60,000 deaths. And the number of patients and deceases is increasing constantly every year.

An important factor to reduce the mortality and morbidity of malignant melanoma patients is the early detection and diagnosis of the disease. It has been reported that the 5-year survival rate reaches a peak of 99% for stage 0, when the tumor is strictly confined to the upper layers of the epidermis, but decreases to values between 25% and 70% in stage 3 of the disease, and it is only between 7% and 20% for stage 4, when the malignant tumor has spread to distant lymph nodes or to organs such as the lungs, liver or brain.

The first step for early detection is visual inspection in order to identify different skin features (moles, blemishes, freckles, other marks on skin) and get noticed of new moles or changes in the existing ones [12]. This can be done by self-inspection but most commonly, it is carried out by a specialist (generally, a dermatologist). Then, diagnostic procedures are applied to analyze the skin tumor and extract its most relevant features, which will be subsequently used for diagnosis purposes. Classical diagnostic procedures include the popular ABCDE method (Asymmetry, Border irregular, Color Uneven, Diameter, Evolving), the Menzies scale, the 7-point checklist, and others [29]. The interested reader is referred to the comprehensive review in [31] for further information. However, all these procedures are time and effort demanding, because in most cases it is difficult to distinguish visually the melanoma from other skin tumors. Furthermore, they are also prone to errors, as they rely completely on human interpretation of images by the medical expert. As a result, they must be often complemented with different types of biopsy, a process that requires significant time and resources. Clearly, there is a need for the development of computer-aided systems to reduce the economic costs and the working burden on the human part for the detection and diagnosis of skin tumors, particularly at early stages. This is the main motivation of the present work.

### 1.2. Manual vs. automatic procedures. Why is this important?

The workflow for automated medical image processing consists of the phases of image acquisition, image pre-processing, image segmentation, feature extraction and classification. In the past, all these steps were carried out in a rather manual way: the image was directly used for visual analysis by the dermatologist for diagnostic and therapeutic purposes. The current trend, however, is to apply computer-assisted image processing techniques to automate the different steps of the process, either fully (automatic diagnosis) or partially (semi-automatic diagnosis).

In this work we focus on image segmentation, one of the key steps of the automated medical image processing workflow. Given one or several medical images of a skin lesion as the input, this step consists of identifying the lesion area for better identification of the skin tumor and its

subsequent classification as either benign or malignant. The common approach to this task in medical practice is highly manual: the dermatologist selects a set of points of the image by clicking with the mouse on the computer screen or any alternative display device. This yields a set of points (called *border points*) assumed to lie on the boundary between the tumor and the background healthy skin. Traditionally, these border points are joined through straight segments, thus yielding a polyline connecting all border points and enclosing the Region of Interest (ROI) of the skin tumor. However, this polyline does not reflect the real boundary curve of the tumor; it is just a rough linear piecewise approximation of the boundary. As such, it cannot be used to analyze different indicators of melanoma, such as asymmetry, border irregularity, or diameter, all of them features analyzed in the classical ABCDE method. Also, this manual procedure does not allow to compute other relevant data such as the perimeter or the area of the tumor, which are important to identify dynamic changes of the tumor shape or size, good indicators of potential melanoma. In conclusion, this manual approach is seriously limited in several respects, and automatic methods are needed to overcome such limitations.

### 1.3. Previous work

There are several papers in the literature describing methods for the analysis of medical skin images. The work in [42] applies color conversion and a nonlinear sigmoid function and double thresholding to compute the boundary edges of the skin lesion. The work in [45] applies noise removal and a fuzzy classifier for detection of melanoma. Thresholding with fuzzy logic has also been applied in [44] to obtain the relevant region of interest of skin tumors. Clustering techniques and wavelets are applied respectively in [38,48] and in [11] for the same purpose. The method in [37] is based on graph theory to categorize the pigmented lesion.

Several computer-assisted solutions for image segmentation have been described in the literature. They include thresholding methods [7, 20], edge-based methods [1], clustering methods [40,47], level set methods [27], and active contours [26]. Other image segmentation methods include graph theory [43] and probabilistic modeling [8].

Artificial intelligence techniques are being increasingly used for the analysis of skin images during the last few decades. They include neural networks [34,36,39], support-vector machines [2], swarm intelligence methods [13,14,18], and hybrid methods [28]. In general, the border curve of the skin tumor is represented as piecewise linear functions or polynomial methods, such as cubic splines, Bézier curves or B-splines. However, it was recently shown that the performance of such methods can be improved by using more general functions [15]. A previous paper by the authors, presented at the SOCO 2020 conference [19], addressed the problem of image segmentation by replacing the polynomial basis functions by rational ones, leading to a significant reduction of the curve degree without penalizing the approximation accuracy. The counterpart is that the rational functions are more difficult than the polynomial ones. To tackle this issue, that paper applied functional networks, a powerful extension of the classical artificial neural networks (ANNs) where the scalar weights in ANNs are replaced by functions. The experimental results showed that this functional network approach outperformed the classical approaches for most of the instances of a given benchmark of medical images.

### 1.4. Aims and main contributions of this work

In spite of its encouraging results, the method presented in our previous conference paper in [19] is seriously limited in one respect (which is also common to all other alternative approaches): the procedure is still *semi-automatic*, in the sense that the input data (i.e., the border points) are selected manually by the dermatologist and given as input to the automatic approximation method. In other words, the generation of the curve from the data points is fully *automatic*, but the

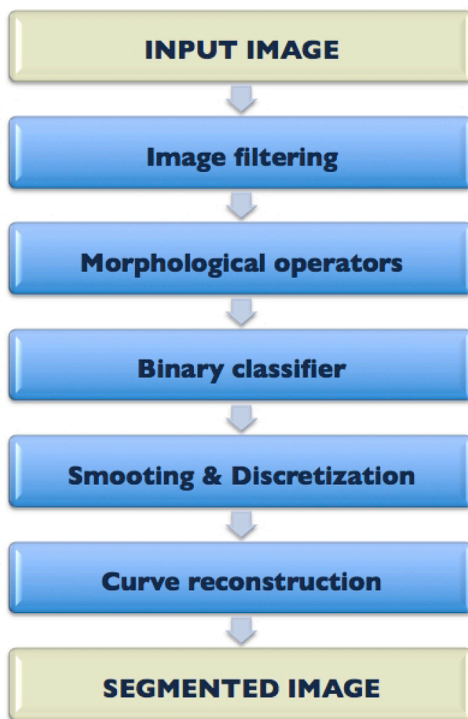


Fig. 1. Graphical pipeline of the proposed method.

generation of such data points is performed literally *by hand*. The present work is aimed at solving this issue.

In particular, we extend our previous work in [19] by making the procedure *fully automatic*. Now, given a medical macroscopic image as an input, we compute automatically both the border points and the curve approximating the border points by following a rational scheme. This task is far from being trivial, however. To automate the whole process, some additional improvements on our previous method in [19] are required. On one hand, we apply filtering on the original medical image in order to remove noise and other undesirable artifacts (e.g., hair). Also, two morphological operators (dilation and erosion) are applied to make the relevant image features more visible, fill small holes, and remove very small islands, so that only substantive features remain. Then, a clustering-based binary classifier method is applied to separate the tumor region from the image background. The boundary between both regions is smoothed and then discretized so that a collection of border points is retrieved in a fully automatic way. Finally, curve reconstruction is applied to compute the boundary curve of the skin tumor. Similar to [19], functional networks are used for curve reconstruction. However, instead of using a rational Bézier curve, as in [19], now we consider a NURBS curve, which is more powerful and versatile. This means that a different type of functional network, called NURBS functional network, is considered. The final output of this process is a NURBS curve enclosing the skin tumor and separating it from the healthy skin background.

The main contributions of this paper are:

- The previous semi-automatic approach for image segmentation in [19] is now replaced by a *fully automatic approach*, in which both the border points and the boundary curve separating the tumor region from the healthy skin background are computed automatically. This feature becomes particularly valuable in situations in which a human expert is not available (e.g., natural disasters, isolated areas), or when extra information is needed for a better diagnosis and more informed medical decision-making (e.g., remote medical diagnosis, inexperienced practitioner).

- This fully automatic image segmentation requires some pre-processing of the original macroscopic images. Our approach includes a *filtering step* to remove noise and other undesirable artifacts (e.g., hair).
- Two *morphological operators* (dilation and erosion) are applied to the filtered image for better visualization of the relevant image features.
- A *clustering-based binary classifier* is included in the method to separate the tumor region from the image background. The resulting boundary is smoother and discretized to obtain the border points.
- Finally, the functional network used in [19] to perform curve reconstruction is now replaced by a (more powerful) NURBS functional network. As a result, the boundary curve is approximated by a NURBS curve instead of a rational Bézier curve, leading to more flexibility (owing to the extra degrees of freedom given by the knots) with a lower polynomial degree.

### 1.5. Structure of this paper

So far, we have discussed the motivation of this paper, pointing out the importance of automatic procedures for image analysis of skin tumors. We have also presented the relevant bibliography in the field, as well as the main contributions of this work. The rest of this paper is organized as follows: Section 2 describes the proposed method in detail. We start with a general overview of the method; then, every individual step is discussed in detail. The computational experiments and the obtained results are reported in Section 3. The paper closes in Section 4 with our conclusions and future work in the field.

## 2. The proposed method

As discussed above, the goal of this paper is to perform image segmentation on medical skin images in a fully automatic way. This means obtaining both the border points and the approximating boundary curve without human intervention. The proposed method to address this issue is presented in this section. Firstly, a brief overview of the method is described. Then, the different steps of the method are discussed in detail.

### 2.1. Overview of the method

The input of the proposed method is a macroscopic medical image,  $\mathcal{I}$ . The method involves several steps, which are graphically summarized in Fig. 1. They are:

1. Filtering is applied to the original medical image  $\mathcal{I}$  to remove noise and other undesirable artifacts (e.g., hair).
2. Two morphological operators (dilation and erosion) are applied to make the relevant image features more visible and remove minor, irrelevant details.
3. A clustering-based binary classifier method is applied to separate the tumor region from the image background.
4. The boundary between both regions is smoothed and discretized to obtain a set of border points.
5. A NURBS functional network is applied to perform curve reconstruction of the border points through a NURBS curve.

As a result of these steps, a segmented image  $S$  from  $\mathcal{I}$  is obtained. Next paragraphs will discuss these steps in detail.

### 2.2. Image filtering

Image filtering is usually applied to skin images in order to remove noise in the images, as well as other undesired artifacts, such as air bubbles or hair [46]. Several types of filters are typically applied to this purpose [35]. They can be roughly classified into two groups: spatial filters and transform domain filters [23]. Methods in the former modify the intensity of each pixel of the image according to the values of the

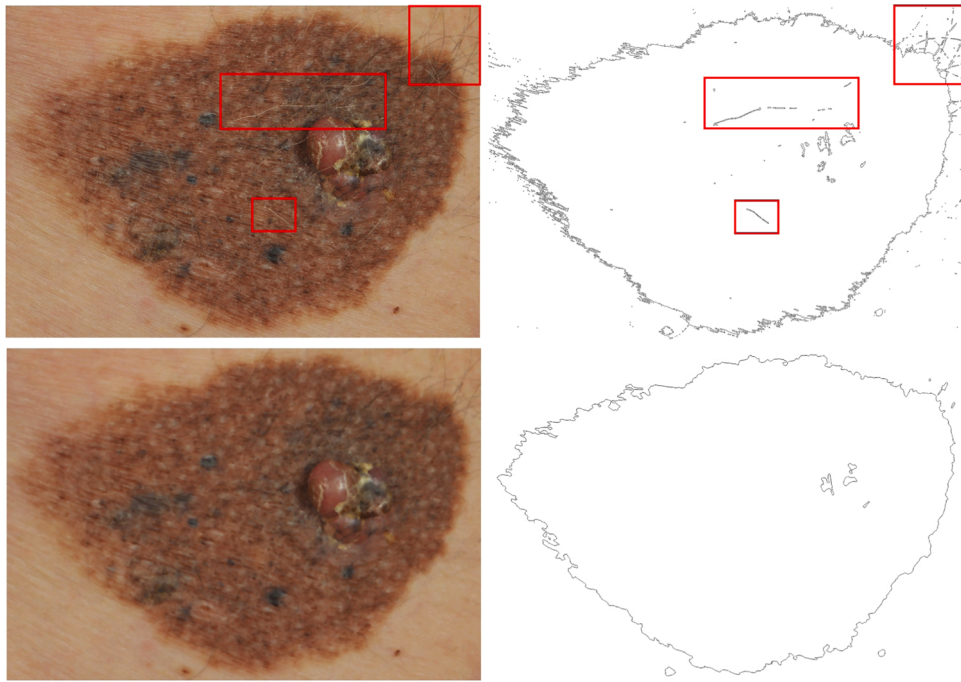


Fig. 2. Illustrative example of application of median filtering for hair removal in a medical skin image: (top-left) original image, with some hair structures enclosed in red; (top-right) most hair structures are clearly visible after edge detection of its morphological binarization; (bottom-left) filtered image; (bottom-right) most hair structures are no longer detected by the edge detection method after filtering.

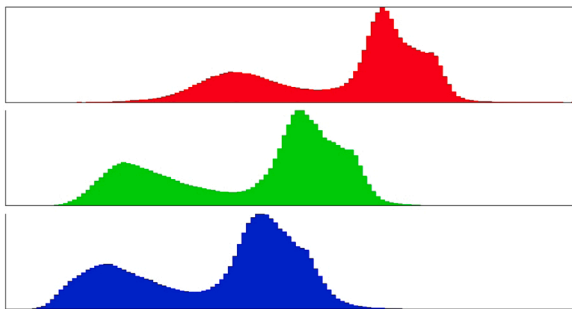


Fig. 3. Histogram of the image in Fig. 5 (top-left) showing the bimodal structure with two peaks for its red, green and blue channel colors. (For interpretation of the references to color in this figure legend, the reader is referred to the web version of this article.)

pixels in the neighborhood of that pixel. Typical examples are the mean filters (arithmetic, geometric, harmonic), the adaptive filters and the order statistical filters. Transform domain filters are mostly based on wavelets. Two previous studies performed a comparative analysis of different filters applied to medical skin images [22,24]. Their results show that the performance of the different filters is strongly dependent on the type of noise, and hence, there is no a single choice for all medical images. Authors in [46] suggested to apply a median filter to medical images of melanoma very similar to those in this work. This is a reasonable choice, as it has been shown that the median filter provides a good trade-off between noise removal and edge preservation. Furthermore, median filtering outperforms Gaussian blur for efficient noise removal whilst preserving edges for small to moderate levels of Gaussian noise. Owing to these reasons, this is the approach we follow here. In particular, we consider a median filter, which replaces the value of each pixel with the median of its neighboring pixels for a window of  $(2r + 1) \times (2r + 1)$  pixels. In this work, we take a value of  $r = 5$ , as it provides good results in all our experiments. However, we remark that it is still an open problem to determine which is the best filtering strategy

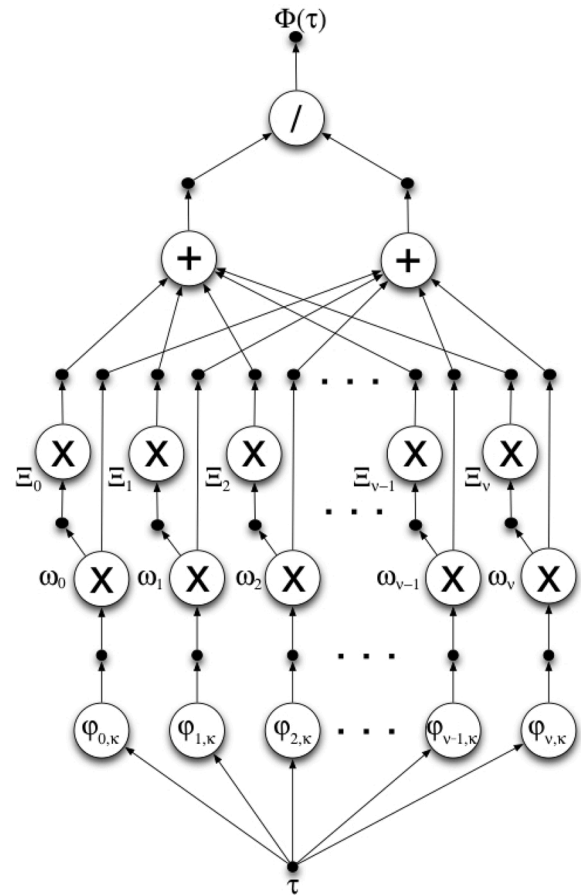
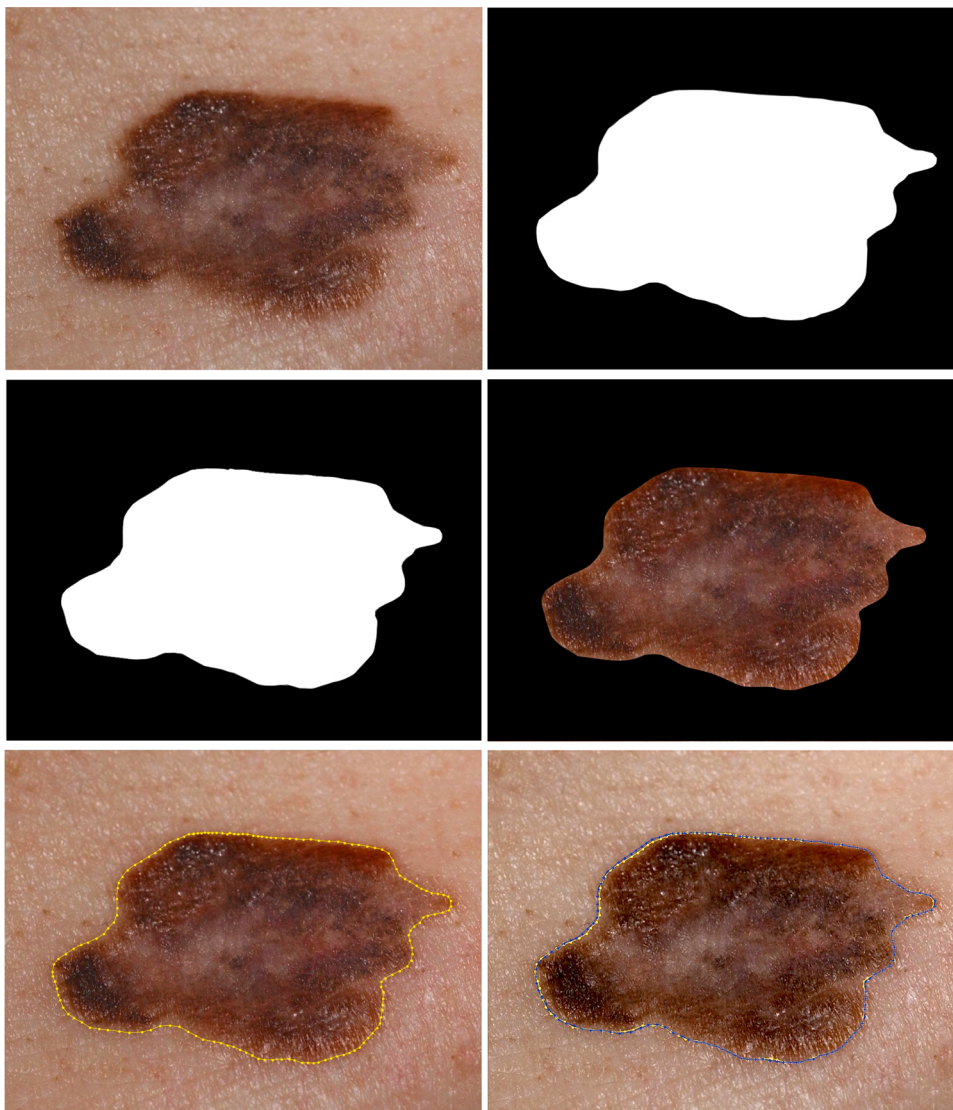


Fig. 4. Functional network for a NURBS curve.



**Fig. 5.** Graphical results for Example 1: (top-left) original image; (top-right) binary mask of the ground truth; (middle-left) binary mask obtained with our method; (middle-right) superposition of the original image and the mask obtained with our method; (bottom-left) border points and boundary curve (in yellow) enclosing the skin tumor area, obtained with our method; (bottom-right) superposition of the border points and boundary curve of the ground truth (in blue) and with our method (in yellow), for easier comparison. (For interpretation of the references to color in this figure legend, the reader is referred to the web version of this article.)

for macroscopic skin images. Clearly, this problem is out of the scope of this paper and will not be addressed here.

Fig. 2 shows an illustrative example of the application of median filtering to hair removal in a macroscopic skin image. The original image (top-left) includes several hairs, such as those enclosed by the three rectangles in red. In Fig. 2 (top-right) we show the results of applying a classical edge detection method (in this particular example, the Canny method, based on the first-order directional Gaussian derivatives) on the morphological binarization of the original image. As the reader can see, the underlying structure of the hairs is still visible at some extent, meaning that the hairs could affect the image segmentation step. Repeating this edge detection method for the filtered image, shown in Fig. 2 (bottom-left), removes the underlying hair structures almost completely, see Fig. 2 (bottom-right).

### 2.3. Morphological operators

Two morphological operators, dilation and erosion, are applied on the filtered image in a rather standard way. The former is applied to make the relevant features of the image more visible and fill in tiny holes in the image due to noise, improper reflections or other visual artifacts. The latter is applied to remove small islands so that only substantive features remain. Together, they improve the visualization of the

meaningful image features, while removing several meaningless features that might remain after the filtering step.

### 2.4. Binary classifier

The automatic detection of border points requires a procedure to discriminate the pixels of the skin lesion from those of the background. In our approach, this task is achieved by using a clustering-based binary classifier. In particular, we consider the Otsu algorithm [30], a very popular method for automatic image thresholding [41]. The algorithm is based on the idea of classifying the pixels in terms of a threshold value  $T$  obtained by minimizing the intra-class intensity variance, defined as a weighted sum of variances of the two classes separated by the threshold  $T$ . Efficient methods for computing a suitable threshold value are described in the literature [25] and currently available in the most popular scientific computing systems.

It is worthwhile to point out that the Otsu algorithm requires a bimodal distribution in the histogram of the image for good performance. This requirement includes to have a deep and pronounced valley between the two peaks of the histogram [25], a condition that usually holds for images containing a clear object surrounded by a relatively uniform background. This situation is also common for many macroscopic skin lesion images. Still, we checked this condition for all images

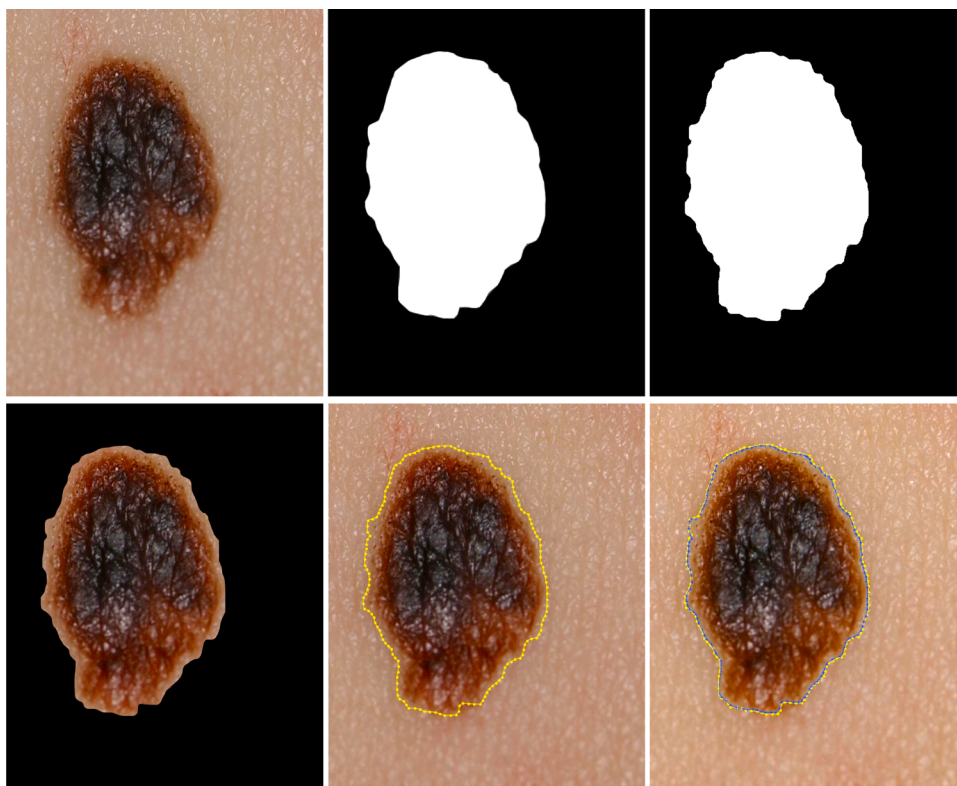


**Fig. 6.** Graphical results for Example 2: (top-left) original image; (top-middle) binary mask of the ground truth; (top-right) binary mask obtained with our method; (bottom-left) superposition of the original image and the mask obtained with our method; (bottom-middle) border points and boundary curve (in yellow) enclosing the skin tumor area, obtained with our method; (bottom-right) superposition of the border points and boundary curve of the ground truth (in blue) and with our method (in yellow), for easier comparison. (For interpretation of the references to color in this figure legend, the reader is referred to the web version of this article.)

considered in this work. An example is given in Fig. 3, where the histogram of a macroscopic melanoma image is shown for illustrative purposes. We remark that the Otsu algorithm was originally intended for gray-level images [30]. However, it can readily be extended to color images by decomposing the image into its different color channels. The image shows the histogram of the color image in Fig. 5 (top-left) in RGB scheme for its red, green and blue channel colors, where the bimodal structure of the histogram with two peaks and a deep valley between them is clearly visible for the three color channels.

Another important consideration is that the performance of the Otsu algorithm is also strongly affected by the size of the object to be segmented, as the performance is degraded for too small sizes. The obvious solution for this problem is to consider a close up of the image to enlarge the size of the region of interest. Finally, the algorithm can also be affected by high levels of noise in the image. Since this step is applied onto the filtered image, not the original one, such a problem does not appear here.

### 2.5. Smoothing and discretization

The output of the previous step is a collection of pixels that belong to the skin lesion. However, the boundary between such pixels and the image background is strongly noisy and irregular. Therefore, smoothing is performed on this boundary curve through a combination of standard morphological operators (to remove small islands and fill in holes) and edge-preserving smoothing techniques. Different techniques can be used for this purpose, including median, bilateral and guided filters. In this work, we use a guided filter, as it has better computational complexity than other types of filters such as median or bilateral, and exhibits good performance in preserving sharp edges while simultaneously avoiding gradient reversal. The detailed analysis and comparison of different filters for smoothing is beyond the scope of this paper and will be part of our future work in the field.

Once smoothing is achieved, we proceed with the discretization of the boundary between the skin lesion and the background. In this work,

we consider an arc-length discretization, where the border points are selected under the equally spaced criterion when advancing on the boundary curve for a prescribed parameter  $h$  accounting for the distance between a given border point and its next neighborhood, where the distance is measured on the boundary of the region of interest. This parameter can be either manually selected by the practitioner or determined automatically when the number of border points is set a priori for the segmentation procedure.

### 2.6. Curve reconstruction

The result of the previous step is a collection of border points obtained in a fully automatic way. Then, curve reconstruction must be applied to obtain a parametric model of the boundary curve. Classical fitting curves are interpolation polynomials (Lagrange, Newton) and cubic splines. However, interpolation is severely affected by noise and outliers and, hence, approximation techniques are more suitable for this problem. Classical approximation techniques for border reconstruction are the free-form parametric curves, primarily based on polynomial schemes such as the popular Bézier and B-spline curves [10,32]. Such schemes can be enhanced by considering extra real parameters called weights, which allow the user to modify the shape of the curve locally by simply changing the weight of one or several poles of the curve without actually moving the location of the poles. This makes it possible to reduce the degree of the curve without penalizing the approximation accuracy. The resulting parametric curve is a rational function instead of a polynomial one.

This rational scheme is more powerful than the polynomial one, but also more difficult to deal with, because extra variables (the weights) are now to be computed. Furthermore, all free variables (data parameters, poles, and weights) are related to each other in a highly nonlinear way [9]. This leads to a difficult continuous multivariate nonlinear optimization problem that cannot be properly solved through traditional mathematical optimization techniques. Some previous papers addressed this problem through swarm intelligence techniques [15,16] which tend

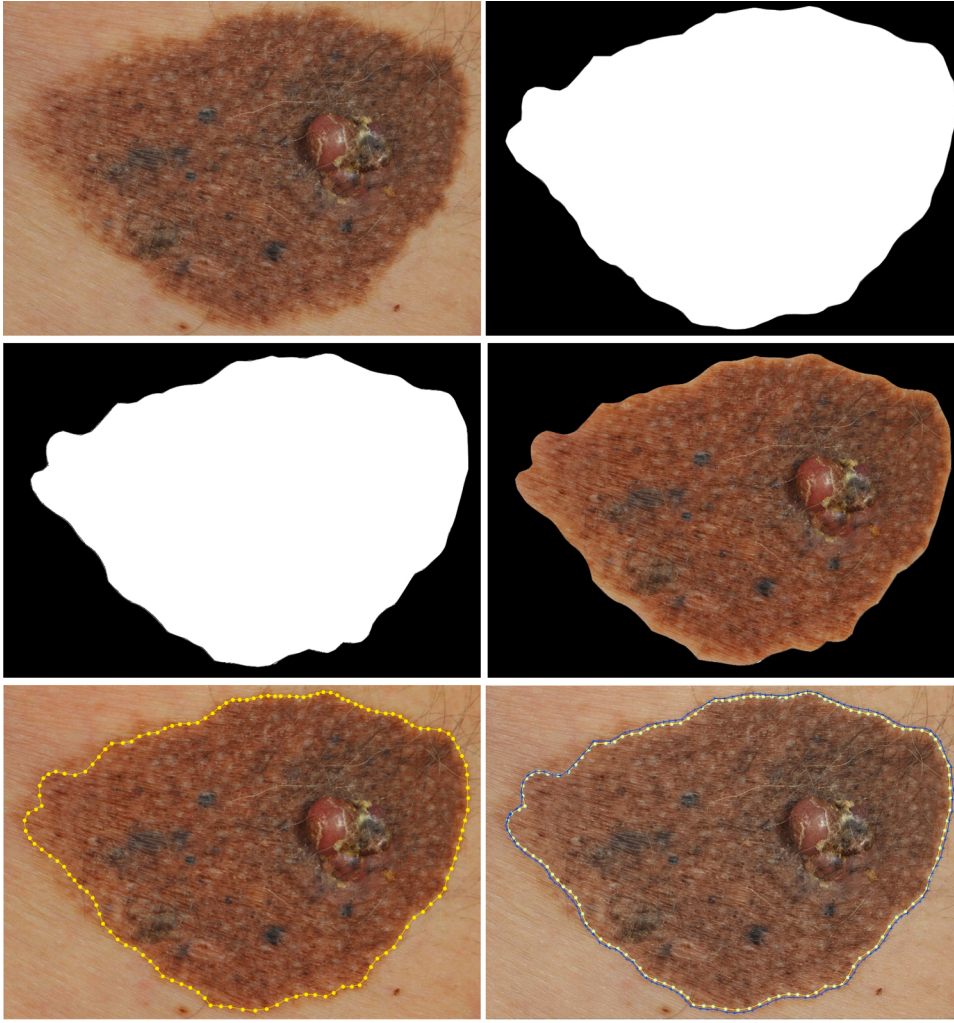


Fig. 7. Graphical results for Example 3: (top-left) original image; (top-right) binary mask of the ground truth; (middle-left) binary mask obtained with our method; (middle-right) superposition of the original image and the mask obtained with our method; (bottom-left) border points and boundary curve (in yellow) enclosing the skin tumor area, obtained with our method; (bottom-right) superposition of the border points and boundary curve of the ground truth (in blue) and with our method (in yellow), for easier comparison. (For interpretation of the references to color in this figure legend, the reader is referred to the web version of this article.)

to be time-consuming and depend on several parameters that have to be properly tuned for good performance. A previous conference paper by the authors presented at SOCO 2020 [19] solves this problem through functional networks, a methodology introduced in [3] to extend the traditional artificial neural networks. The differential factor of functional networks is that the scalar weights that are typical in ANNs are replaced by functions, leading to a new methodology that is more general and more powerful than the ANNs. The counterpart is that the learning process in functional networks requires to solve a set of functional equations [6], which is arguably more difficult than the set of equations derived from the neural networks learning process.

The conference paper in [19] already discussed the main components of a functional network along with the main differences between neural networks and functional networks, so these aspects are omitted here to avoid unnecessary duplication of material. Instead, in this paper we focus on the different architecture of the functional networks used in the previous conference paper and in this work.

In the previous paper we considered rational Bézier curves, and introduced a functional network replicating their mathematical structure. In this work we perform data fitting of the border points through NURBS. This requires a new network architecture, shown in Fig. 4, to account for the new variables and basis functions, as explained in next paragraphs.

### 2.6.1. B-spline basis functions

Let  $\mathcal{U} = \{u_0, u_1, u_2, \dots, u_{r-1}, u_r\}$  be a nondecreasing sequence of real numbers called *knots*.  $\mathcal{U}$  is called the *knot vector*. The *i*th *B-spline basis*

function  $\varphi_{i,\kappa}(\tau)$  of order  $\kappa$  (or equivalently, degree  $\kappa - 1$ ) is defined by the recurrence relation

$$\varphi_{i,1}(\tau) = \begin{cases} 1 & \text{if } u_i \leq \tau < u_{i+1} \\ 0 & \text{otherwise} \end{cases} \quad (1)$$

with  $i = 0, \dots, r - 1$  and

$$\varphi_{i,\kappa}(\tau) = \frac{\tau - u_i}{u_{i+\kappa-1} - u_i} \varphi_{i,\kappa-1}(\tau) + \frac{u_{i+\kappa} - \tau}{u_{i+\kappa} - u_{i+1}} \varphi_{i+1,\kappa-1}(\tau) \quad (2)$$

for  $\kappa > 1$ . Note that *i*th B-spline basis function of order 1,  $\varphi_{i,1}(\tau)$ , is a piecewise constant function with value 1 on the semi-open interval  $[u_i, u_{i+1})$ , called the *support* of  $\varphi_{i,1}(\tau)$ , and zero elsewhere. This support can be either an interval or reduce to a point, as knots  $u_i$  and  $u_{i+1}$  must not necessarily be different. If necessary, the convention  $\frac{0}{0} = 0$  in Eq. (2) is applied. Any basis function of order  $\kappa > 1$ ,  $N_{i,\kappa}(\tau)$ , is a linear combination of two consecutive functions of order  $\kappa - 1$ , where the coefficients are linear polynomials in  $\tau$ , such that its order (and hence its degree) increases by 1. Simultaneously, its support is the union of the (partially overlapping) supports of the former basis functions of order  $\kappa - 1$  and, consequently, it usually enlarges.

### 2.6.2. NURBS curve

A *NURBS curve* of order  $\kappa$  is a rational parametric curve given by:

$$\Phi(\tau) = \frac{\sum_{i=0}^v \Xi_i \omega_i \varphi_{i,\kappa}(\tau)}{\sum_{i=0}^v \omega_i \varphi_{i,\kappa}(\tau)} \quad (3)$$

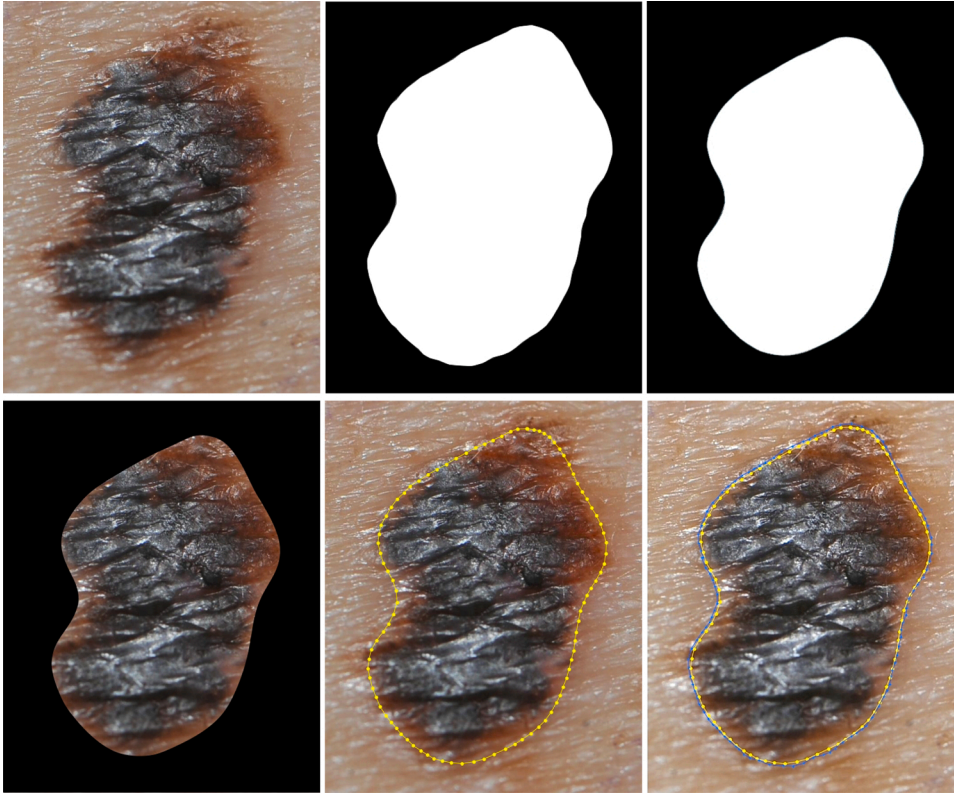


**Fig. 8.** Graphical results for Example 4: (top-left) original image; (top-middle) binary mask of the ground truth; (top-right) binary mask obtained with our method; (bottom-left) superposition of the original image and the mask obtained with our method; (bottom-middle) border points and boundary curve (in yellow) enclosing the skin tumor area, obtained with our method; (bottom-right) superposition of the border points and boundary curve of the ground truth (in blue) and with our method (in yellow), for easier comparison. (For interpretation of the references to color in this figure legend, the reader is referred to the web version of this article.)

where  $\{\Xi_i\}_i$  are vector coefficients called *poles*, which determine the shape of the curve,  $\varphi_{i,\kappa}(\tau)$  are the B-spline basis functions defined above and  $\{\omega_i\}_i$  are weights associated with the poles  $\{\Xi_i\}_i$ ,  $i = 0, \dots, \nu$ . Without loss of generality, the parameter  $\tau$  can be assumed to take values on the interval  $[0, 1]$ . For a proper definition of a NURBS curve in Eq. (3), the following relationship must hold:  $r = \kappa + \nu$  (see [32] for further details).

### 2.6.3. The NURBS functional network

The functional network in Fig. 4 is particularly tailored to replicate the mathematical structure of a NURBS curve, given by Eq. (3). The workflow of the network proceeds upwardly: taking as input a parameter value  $\tau$  and an order  $\kappa$ , the functional network computes the values of the basis functions  $\varphi_{i,\kappa}(\tau)$  at  $\tau$  and then the terms  $\omega_i \varphi_{i,\kappa}(\tau)$  and  $\Xi_i \omega_i \varphi_{i,\kappa}(\tau)$  ( $i = 0, \dots, \nu$ ). Summation on index  $i$  is applied to both expressions thus yielding the denominator and numerator of (3), respectively. Then, the quotient operator is applied to obtain the final expression of the curve,  $\Phi(\tau)$ .

It is worthwhile to mention three interesting features of this functional network:

- The network includes two different types of  $\times$  operators: a scalar (dot) product for the multiplication by the weights  $\omega_i$  and the component-wise (Hadamard) product for the multiplication by the poles  $\Xi_i$ .
- The poles  $\Xi_i$  play a similar role to that of the weights in neural functions, in the sense that our functional network with  $\nu$ -dimensional vectors as weights might be understood as  $\nu$  parallel functional networks with scalar weights given by the  $\nu$  components of the poles.
- We finally remark that the architecture of the lower layers of our functional network makes it well suited for (partial) bottom-up parallelization. For instance, the computation of the B-spline basis functions can be parallelized. The same applies for the scalar and Hadamard products in the next layers upwards of the network.

### 2.6.4. Computing the border points with the NURBS functional network

Given the sequence of  $\mu$  border points,  $\{\xi_j\}_{j=1,\dots,\mu}$ , obtained in previous steps, the functional network in Fig. 4 is applied to reconstruct the border curve with NURBS. In this work, we consider a chord-length parameterization of the border points, given by:

$$\tau_1 = 0; \quad \tau_\mu = 1; \quad \tau_j = \tau_{j-1} + \frac{|\xi_j - \xi_{j-1}|}{\sum_{k=2}^{\mu} |\xi_k - \xi_{k-1}|} \quad (j = 2, \dots, \mu - 1) \quad (4)$$

while the knots are computed by the averaging method [32]. Then, we perform parametric learning of the functional network, a step that requires to determine the scalar and vector weights of the network. To this aim, we perform least-squares minimization of the functional:

$$\Psi = \sum_{j=1}^{\mu} (\xi_j - \Phi(\tau_j))^2 = \sum_{j=1}^{\mu} \left( \xi_j - \frac{\sum_{i=0}^{\nu} \Xi_i \omega_i \varphi_{i,\kappa}(\tau_j)}{\sum_{i=0}^{\nu} \omega_i \varphi_{i,\kappa}(\tau_j)} \right)^2 \quad (5)$$

with parametric values  $\{\tau_j\}$ ,  $j = 1, \dots, \mu$  obtained from Eq. (4). It is important to note that the scalar and the vector weights of the network are strongly related to each other in a complicated nonlinear way, so they cannot be computed independently (in other words, the set of variables of this optimization problem is not linearly separable), so classical mathematical optimization techniques fail to solve the problem. This is the main reason (albeit not the only one) why we apply functional networks in this work.

The expression (5) yields a system of equations (called *normal equations*) that can be simplified to a linear system solved by either LU decomposition or by Singular Value Decomposition (SVD) (see [33] for details). In this work, we apply SVD as it provides the best numerical solution in the sense of least-squares for those cases in which no exact solution can be obtained.

The final output of this step is the boundary curve separating the skin tumor area from the background healthy skin. This boundary curve is expressed mathematically as a smooth rational parametric function, in particular, a NURBS curve, which is the standard *de facto* in fields such

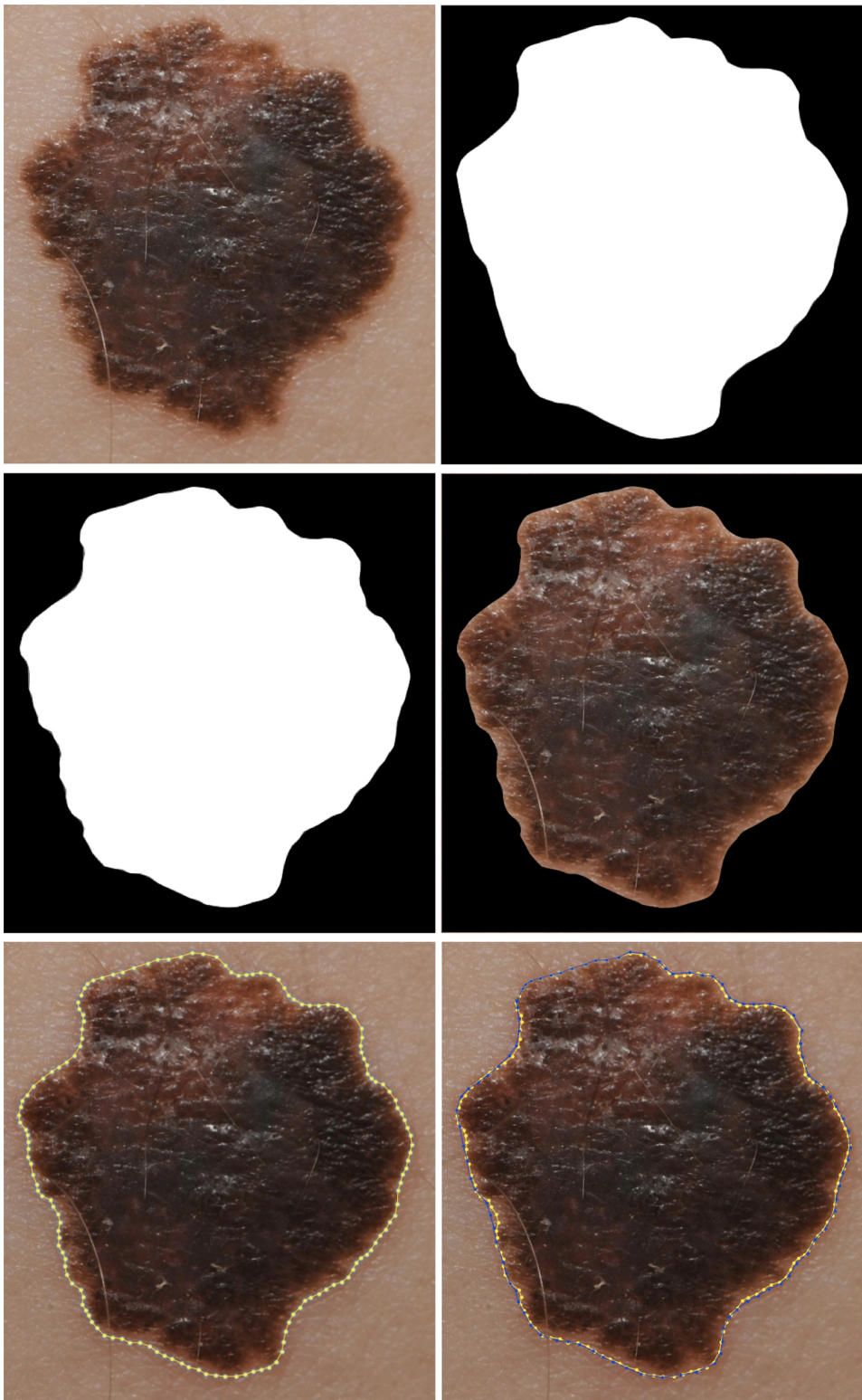


**Fig. 9.** Graphical results for Example 5: (top-left) original image; (top-right) binary mask of the ground truth; (middle-left) binary mask obtained with our method; (middle-right) superposition of the original image and the mask obtained with our method; (bottom-left) border points and boundary curve (in yellow) enclosing the skin tumor area, obtained with our method; (bottom-right) superposition of the border points and boundary curve of the ground truth (in blue) and with our method (in yellow), for easier comparison. (For interpretation of the references to color in this figure legend, the reader is referred to the web version of this article.)

as computer graphics, industrial and manufacturing engineering, computational biology, biomedical engineering, and many others.

### 2.7. Implementation issues

The computational work in this paper has been carried out on a 3.7 GHz Intel Core i7 processor PC with 16 GB of RAM. The source code of the different steps of the method has been mainly implemented by the

authors in *Matlab*, version 2018b running on Windows 10 OS. In our opinion, *Matlab* is a very suitable tool for this work, as it includes several libraries and functions for the different tasks involved in this method, including excellent visualization tools and optimized code for image processing. Furthermore, it is possible to generate C++ code from native code in *Matlab* for standalone applications using a powerful set of compilers and other additional tools. Solving the functional equations for the functional network requires a different approach: in this work,

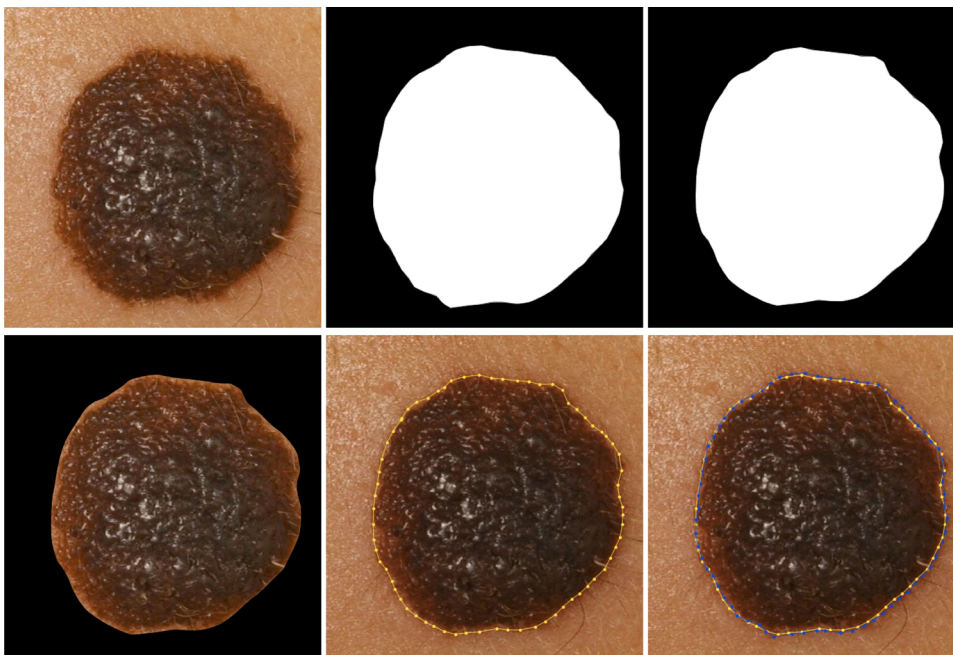


**Fig. 10.** Graphical results for Example 6: (top-left) original image; (top-middle) binary mask of the ground truth; (top-right) binary mask obtained with our method; (bottom-left) superposition of the original image and the mask obtained with our method; (bottom-middle) border points and boundary curve (in yellow) enclosing the skin tumor area, obtained with our method; (bottom-right) superposition of the border points and boundary curve of the ground truth (in blue) and with our method (in yellow), for easier comparison. (For interpretation of the references to color in this figure legend, the reader is referred to the web version of this article.)

**Table 1**

Numerical results of the proposed method for the six examples (in rows) in this paper: (in columns, from left to right): number of example, number of border points, RMSE of the curve reconstruction process, perimeter of the boundary curve, its absolute error and relative error (in percentage), and area enclosed by the boundary curve, its absolute error and relative error (in percentage).

Ex.	$\mu$	RMSE	Perimeter (proposed method)			Area (proposed method)		
			Value	Abs. error	Rel. error	Value	Abs. error	Rel. error
1	154	5.76E-3	24.218	0.218	0.89%	36.121	1.191	3.19%
2	162	3.18E-2	21.071	0.264	1.26%	29.477	1.258	4.45%
3	143	2.77E-2	29.827	1.229	3.95%	61.131	1.657	2.63%
4	116	1.03E-2	25.434	0.801	3.05%	45.364	2.328	4.88%
5	149	4.24E-3	29.085	0.386	1.32%	57.469	1.107	1.92%
6	70	8.76E-3	25.540	0.443	1.74%	49.837	0.638	1.28%

we rely on a set of libraries for functional equations developed in *Mathematica* years ago [4,5] using functional programming. Finally, some routines from the *Matlab* toolbox for computer graphics and different geometry developed by some of the authors and described in [17] have been applied to optimize the computation of both the B-spline basis functions and the knot vectors, and for border points parameterization.

### 3. Computational experiments and results

The proposed method has been applied to several examples of medical images of skin tumors. In this paper, we consider two different benchmarks, comprised of four and two macroscopic medical images of skin tumors obtained from public repositories of medical images freely available for research purposes [21]. The first benchmark consists of the four macroscopic medical images shown in our previous conference paper, labelled now as Example 1 to Example 4. The corresponding graphical results for these four examples are displayed in Figs. 5 to 8, respectively. The second benchmark corresponds to two extra macroscopic medical images not used in our previous conference paper and obtained from the digital image archive of the Department of Dermatology of the University Medical Center of Groningen (The Netherlands). They are labelled as Examples 5 and 6, and graphically displayed in Figs. 9 and 10, respectively.

For each figure of every example, six images are shown: firstly, the original medical image is shown in the top-left image. Then, the binary

mask corresponding to the ground truth is displayed. Application of the steps of our method described in Sections 2.2–2.4 yields a new binary mask, separating the skin lesion from the background. The binary mask is then smoothed as described in Section 2.5, leading to the smooth binary mask shown as the third image of each figure. A superposition of the original image and the mask obtained with our method is shown as the fourth image for better visualization purposes. Applying the arc-length discretization step briefly described in Section 2.5 yields a set of border points, depicted as small yellow circles in the fifth image of each figure. Then, the NURBS functional network is applied to reconstruct the boundary curve from these border points. The output is the NURBS curve shown as a solid yellow line in the same image. Finally, a superposition of the border points and the boundary curve of the ground truth (in blue) and obtained with our method (in yellow) is shown in last image of each figure for easier visual comparison of the ground truth and our results.

A simple visual observation of the images in the paper shows that the method performs very well: all intermediate and final outputs (the binary mask, the border points, and the final boundary curve) match the corresponding skin tumor area with good visual accuracy. Also, the visual comparison of our results and the ground truth for both the binary masks and the border points and boundary curves show that our results are very close to the ground truth in all examples in the benchmark. We have shown these results to three proficient dermatologists, who gave us a very positive feedback after a visual assessment of the images shown in the paper. They mentioned that the results are appealing, albeit not

really extraordinary in terms of accuracy. However, it must be remarked here that all these images have been obtained in a *fully automatic way*, i. e., without human intervention in any of the steps of the method. This feature impressed them, as they expected the procedure to include some kind of human supervision during the process in order to modify some parameters, and introduce some modifications *on the fly*, as it is commonly done with current technology. Also, in their opinion, the results are good enough to be used for clinical practice.

This visual observation is also confirmed numerically through different metrics. The first one concerns the accuracy of the fitting error for the curve reconstruction process from the border points. This is computed by the least-squares error in Eq. (5). However, this functional does not take into account the number of border points and thus, the error increases with the number of data. To fix this, we consider the root-mean square error (RMSE) given by:  $RMSE = \sqrt{\frac{\sum \mu}{\mu}}$ , where  $\mu$  denotes the number of border points. For additional metrics, we have asked this group of three dermatologists to apply the standard procedure in clinical practice to our examples independently. After obtaining the three independent results, we asked them to reach a consensus decision to determine the ground truth in order to obtain a reference value for our results for comparative purposes. To this aim, we computed the perimeter of the boundary curve obtained with the proposed method as well as the area of the region enclosed by the curve. Then, we compare such values with those of the ground truth to compute the absolute and the relative error. It is important to remark here that, similar to the conference paper, the six figures are *not* equally scaled; some of them have been resized for better visualization. This means that the sizes, perimeters and areas of each example cannot be compared with each other, only with the corresponding ground truth.

Table 1 reports the numerical results of this comparison. For each example in the benchmark (arranged in rows), the table shows the following data (in columns): number of the example, number of border points obtained with the proposed method, RMSE of the curve reconstruction process, perimeter of the boundary curve obtained with the proposed method, its absolute error and relative error (in percentage), and area enclosed by the boundary curve, its absolute error and relative error (in percentage).

Some interesting observations can be remarked from the results in the table:

- The RMSE for the six examples is of order of  $10^{-2}$ – $10^{-3}$ , depending on the particular example. This small value is a good indicator that the method performs well, being able to reconstruct the boundary curve with very good accuracy.
- In general, the proposed method yields boundary curves with slightly shorter length and smaller area than the ground truth. This can be explained by the fact that the boundary curves in standard clinical practice are comprised of linear segments connected together at the border points (i.e., a polyline), while generally the actual boundary curve is not a piecewise linear function. On the contrary, our method uses a NURBS curve, which can be chosen to be smooth. In addition, NURBS curves are widely used for data fitting owing to their ability to replicate the underlying shape of data, which means passing very near to the data points.
- The only exception to the previous remark is given by Example 2, where the situation is the opposite. We speculate that this behavior can be attributed to the particular pattern of color at the boundary of the skin tumor of this image, which exhibits several levels of intensity for the brown color. In such situation, the filtering strategy applied in this paper might not reveal a clear boundary, leading to a sub-optimal threshold value for the binary classifier step described in Section 2.4. Fixing this problem would probably require an additional step for contrast enhancement, which is out of the scope of this paper and will be part of our future work in the field.

- The relative error values of our method vary from 0.89% to 3.95% for the perimeter of the curves, and from 1.28% to 4.88% for the enclosed areas, well within what is considered acceptable for clinical practice. These small percentage values validate the good performance of the method for image segmentation.

In this work, we do not include any comparative analysis with other methods for medical image segmentation described in the literature. The fact that our method is fully automatic makes it hard to carry out a fair comparison with alternative methods, which typically follow a semi-automatic approach. In our opinion, it is not fair to compare different methods based solely on their performance; human intervention is also an important factor in the process. When professional practitioners try to improve the image quality, they use their own experience and a deep knowledge of the technology at their disposal in order to select the most suitable technique with proper setting values for optimal performance. This performance is often based on the visual quality they perceive from the images, which can even vary depending on the visual acuity of the practitioner. This shows that human intervention is a complex process involving previous experiences, cognitive factors, psycho-physiological factors, ambient factors, and many others. It is not realistic to expect that this complex process can be fully done automatically to the same level of detail.

#### 4. Conclusions and future work

This work extends a previous paper by the authors presented at SOCO 2020 conference that introduced an image segmentation method for medical skin images through functional networks. Although the method performed well, it followed a semi-automatic approach involving manual and automatic operations. In particular, the border points were selected manually by a dermatologist, while the curve reconstruction from such border points was carried out automatically. The present work extends this methodology significantly in order to make image segmentation a fully automatic process. To this aim, the proposed method includes five new relevant features: (1) a filtering strategy for removal of noise, hair and other artifacts; (2) two morphological operators for image enhancement; (3) a clustering-based binary classifier to separate the skin tumor from the image background; (4) a smoothing and discretization process to obtain the border points; and (5) a curve reconstruction method from the border points using NURBS curves. This last feature requires a new type of functional network (called NURBS functional network), especially designed for this task. This new method is applied to a benchmark of four macroscopic skin images already used in the previous conference paper, and another benchmark of two macroscopic images obtained from a public medical repository of skin tumors and not included in our conference paper. Our visual and numerical results show that the method performs very well. The method yields segmented images which, when presented to experienced dermatologists, were assessed of reasonable quality and well suited for clinical practice. Furthermore, the numerical results shows RMSE of order  $10^{-2}$ – $10^{-3}$  for the boundary curve reconstruction from the border points, along with relative errors less than 5% for the perimeters and enclosed areas of the boundary curves with respect to the ground truth.

Of course, the methodology introduced in this work also comes with some limitations and can be further extended in several different ways. On one hand, the method is restricted exclusively to image segmentation, one of the steps of the whole medical image analysis pipeline. Other steps and tasks, such as image enhancement, image restoration, or feature extraction, are still to be addressed in order to obtain a fully automatic procedure for medical diagnosis and classification of the skin tumors. Also, in this paper we do not address the subproblem of selecting the best filtering strategy for optimal performance. This will be part of our future work in the field. Another future topic of research will be to improve the binary classifier used here. Different ideas can be used in

this regard, such as logistic regression, support vector machines, decision trees, perceptron neural network, naive Bayes, or random forest. On the other hand, the method is restricted to macroscopic images. We plan to extend this methodology to the case of microscopic images, where some additional steps (e.g., contrast enhancement, black frame removal) are required along with the modification of the current ones for better performance. The application of all those new techniques for the automatic diagnosis of skin tumors as benign or malignant and the identification of the particular type of skin tumor for each image are also part of our future goals in the field.

### Conflict of interest

The authors declare that there is no conflict of interests regarding the publication of this article. Any commercial identity mentioned in this paper is cited solely for scientific purposes.

### Declaration of Competing Interest

The authors report no declarations of interest.

### Acknowledgments

Akemi Gálvez and Andrés Iglesias have received funding from the project PDE-GIR of the European Union's Horizon 2020 research and innovation programme under the Marie Skłodowska-Curie grant agreement no. 778035, and from the project TIN2017-89275-R funded by MCIN/AEI /10.13039/501100011033/FEDER "Una manera de hacer Europa". Iztok Fister acknowledges financial support from the Slovenian Research Agency (Grant No. P2-0041). Iztok Fister Jr. acknowledges financial support from the Slovenian Research Agency (Grant No. P2-0057).

### References

- [1] A.A. Abbas, X. Guo, W.H. Tan, H.A. Jalab, Combined spline and B-spline for an improved automatic skin lesion segmentation in dermoscopic images using optimal color channel, *J. Med. Syst.* 38 (2014) 80.
- [2] S. Bakheet, An SVM framework for malignant melanoma detection based on optimized HOG features, *Computation* 5 (2017) 4.
- [3] E. Castillo, Functional networks, *Neural Process. Lett.* 7 (1998) 151–159.
- [4] E. Castillo, A. Iglesias, A package for symbolic solution of real functional equations of real variables, *Aequationes Math.* 54 (1–2) (1997) 181–198.
- [5] E. Castillo, A. Iglesias, A. Cobo, A package for symbolic solution of functional equations. Proc. of the First International Mathematica Symposium, IMS-95, Computational Mechanics Publications, Southampton, UK, 1995, pp. 85–92.
- [6] E. Castillo, A. Iglesias, R. Ruiz-Cobo, *Functional Equations in Applied Sciences*, Elsevier, Amsterdam, 2005.
- [7] M.E. Celebi, H. Iyatomi, G. Schaefer, W.V. Stoecker, Lesion border detection in dermoscopy images, *Comp. Med. Imaging Graph.* 33 (2) (2009) 148–153.
- [8] M.E. Celebi, H.A. Kingravi, H. Iyatomi, Y. Alp Aslandogan, W.V. Stoecker, R. H. Moss, J.M. Malter, J.M. Grichnik, A.A. Marghoob, H.S. Rabinovitz, S. W. Menzies, Border detection in dermoscopy images using statistical region merging, *Skin Res. Technol.* 14 (2008) 347–353.
- [9] P. Dierckx, *Curve and Surface Fitting with Splines*, Oxford University Press, Oxford, 1993.
- [10] G. Farin, *Curves and Surfaces for CAGD*, 5th ed., Morgan Kaufmann, San Francisco, 2002.
- [11] N. Fassihi, J. Shanbehzadeh, H. Sarrafzadeh, E. Ghasemi, Melanoma diagnosis by the use of wavelet analysis based on morphological operators, Proc. of the Int. Conf. of Engineers and Computer Scientists, IMECS 2011 (2011) 193–196.
- [12] R.J. Friedman, D.S. Rigel, A.W. Kopf, Early detection of malignant melanoma: the role of physician examination and self-examination of the skin, *Cancer J. Clin.* 35 (3) (1985) 130–151.
- [13] A. Gálvez, I. Fister, I. Fister Jr., E. Osaba, J. Del Ser, A. Iglesias, Automatic fitting of feature points for border detection of skin lesions in medical images with bat algorithm, *Stud. Comput. Intell.* 798 (2018) 357–368.
- [14] A. Gálvez, I. Fister, E. Osaba, I. Fister Jr., J. Del Ser, A. Iglesias, Hybrid modified firefly algorithm for border detection of skin lesions in medical imaging. Proc. of IEEE Congress on Evolutionary Computation, IEEE CEC 2019, IEEE Computer Society Press, Los Alamitos, CA, 2019, pp. 111–118.
- [15] A. Gálvez, I. Fister Jr., E. Osaba, I. Fister, J. Del Ser, A. Iglesias, Computing rational border curves of melanoma and other skin lesions from medical images with bat algorithm, Proc. of ACM Genetic and Evolutionary Computation Conference, ACM GECCO 2019 (2019) 1675–1682.
- [16] A. Gálvez, I. Fister, I. Fister Jr., E. Osaba, J. Del Ser, A. Iglesias, Cuckoo search algorithm for border reconstruction of medical images with rational curves, *Lect. Notes Comput. Sci.* 11655 (2019) 320–330.
- [17] A. Gálvez, A. Iglesias, Numerical-symbolic Matlab toolbox for computer graphics and differential geometry, *Lect. Notes Comput. Sci.* 3482 (2005) 502–511.
- [18] A. Gálvez, A. Iglesias, Memetic improved cuckoo search algorithm for automatic B-spline border approximation of cutaneous melanoma from macroscopic medical images, *Adv. Eng. Informatics* 43 (2020) 101005.
- [19] A. Gálvez, I. Fister, I. Fister Jr., A. Iglesias, Functional networks for image segmentation of cutaneous lesions with rational curves, Proc. of the 15th Int. Conf. on Soft Computing Models in Industrial and Environmental Applications, SOCO 2020. Advances in Intelligent Systems and Computing, 1268 (2020) 780–789.
- [20] R. Garnavi, M. Aldeen, M.E. Celebi, G. Varigos, S. Finch, Border detection in dermoscopy images using hybrid thresholding on optimized color channels, *Comput. Med. Imaging Graph.* 35 (2) (2011) 105–115.
- [21] I. Giotis, N. Molders, S. Land, M. Biehl, M.F. Jonkman, N. Petkov, MED-NODE: a computer-assisted melanoma diagnosis system using non-dermoscopic images, *Expert Syst. Appl.* 42 (2015) 6578–6585.
- [22] R.J. Hemalatha, B. Babu, J.A. Dhivya, T.R. Thamizhvan, J.E.J.R. Chandrasekaran, A comparison of filtering and enhancement methods in malignant melanoma images, Proc. of IEEE International Conference on Power, Control, Signals and Instrumentation Engineering, ICPCSI-2017 (2017) 2704–2710.
- [23] A.N. Hoshyar, A. Al-Jumaily, A.N. Hoshyar, The beneficial techniques in preprocessing step of skin cancer detection system comparing, Proc. of Int. Conf. on Medical and Rehabilitation Robotics and Instrumentation, PRIDE. Procedia Computer Science, vol. 42 (2014) 25–31.
- [24] A.N. Hoshyar, A. Al-Jumaily, A.N. Hoshyar, Comparing the performance of various filters on skin cancer images, Proc. of Int. Conf. on Medical and Rehabilitation Robotics and Instrumentation, PRIDE. Procedia Computer Science, vol. 42 (2014) 32–37.
- [25] J. Kittler, J. Illingworth, On threshold selection using clustering criteria, *IEEE Trans. Syst. Man Cybern.* 15 (5) (1985) 652–655.
- [26] Z. Ma, J.M. Tavares, A novel approach to segment skin lesions in dermoscopic images based on a deformable model, *IEEE J. Biomed. Health Informatics* 20 (2016) 615–623.
- [27] D.A. Machado, G. Giraldo, A.A. Novotny, Multi-object segmentation approach based on topological derivative and level set method, *Integr. Comput.-Aided Eng.* 18 (2011) 301–311.
- [28] A. Murugan, S.A.H. Nair, K.P.S. Kumar, Detection of skin cancer using SVM, random forest and kNN classifiers, *J. Med. Syst.* 43 (2019) 269.
- [29] F. Nachbar, W. Stolz, T. Merkle, A.B. Cognetta, T. Vogt, M. Landthaler, P. Bilek, O. Braun-Falco, G. Plewig, The ABCD rule of dermatoscopy. High prospective value in the diagnosis of doubtful melanocytic skin lesions, *J. Am. Acad. Dermatol.* 30 (4) (1994) 551–559.
- [30] N. Otsu, A threshold selection method from gray-level histograms, *IEEE Trans. Syst. Man Cybern.* 9 (1) (1979) 62–66.
- [31] S. Pathan, K.G. Prabhu, P.C. Siddalingaswamy, Techniques and algorithms for computer aided diagnosis of pigmented skin lesions – a review, *Biomed. Signal Process. Control* 39 (2018) 237–262.
- [32] L. Piegl, W. Tiller, *The NURBS Book*, Springer Verlag, Berlin Heidelberg, 1997.
- [33] W.H. Press, S.A. Teukolsky, W.T. Vetterling, B.P. Flannery, *Numerical Recipes*, 2nd ed., Cambridge University Press, Cambridge, 1992.
- [34] M. Rajab, M. Woolfson, S. Morgan, Application of region-based segmentation and neural network edge detection to skin lesions, *Comput. Med. Imaging Graph.* 28 (2004) 61–68.
- [35] R. Ramya Ravi, R.S. Vinod Kumar, N. Shanila, Artifacts removal in melanoma using various preprocessing filters, *Int. J. Eng. Technol.* 7 (2018) 104–107.
- [36] N. Razmjooy, F.R. Sheykahmad, N. Ghadimi, A hybrid neural network – world cup optimization algorithm for melanoma detection, *Open Med.* 13 (2018) 9–16.
- [37] M. Sadeghi, M. Razmara, M. Ester, T.K. Lee, M.S. Atkins, Graph-based pigment network detection in skin images, *Proc. SPIE* 7623 (2010) 762312.
- [38] F.S. Saleh, R. Azmi, Automated lesion border detection of dermoscopy images using spectral clustering, Proc. of 2nd International Conference on Pattern Recognition and Image Analysis, IPRIA 2015 (2015).
- [39] L. Sanchez-Reyes, J. Rodriguez-Resendiz, S. Salazar-Colores, G. Avecilla-Ramirez, G. Perez-Soto, A high-accuracy mathematical morphology and multilayer perceptron-based approach for melanoma detection, *Appl. Sci.* 10 (2020) 1098.
- [40] P. Schmid, Segmentation of digitized dermoscopic images by two-dimensional color clustering, *IEEE Trans. Med. Imaging* 18 (2) (1999) 164–171.
- [41] M. Sezgin, B. Sankur, Survey over image thresholding techniques and quantitative performance evaluation, *J. Electron. Imaging* 13 (2004) 146–165.
- [42] L. Xu, M. Jackowski, A. Goshtasby, D. Roseman, S. Bines, C. Yu, A. Dhawan, A. Huntley, Segmentation of skin cancer images, *Image Vision Comput.* 17 (1) (1999) 65–74.
- [43] X. Yuan, N. Situ, G. Zouridakis, A narrow band graph partitioning method for skin lesion segmentation, *Pattern Recogn.* 42 (2009) 1017–1028.
- [44] M.E. Yuksel, M. Borlu, Accurate segmentation of dermoscopic images by image thresholding based on type-2 fuzzy logic, *IEEE Trans. Fuzzy Syst.* 17 (2009) 976–982.
- [45] E. Zagrouba, W. Barhoumi, A preliminary approach for the automated recognition of malignant melanoma, *Image Anal. Stereol.* 23 (2) (2011) 121–135.

- [46] N.S. Zghal, N. Derbel, Melanoma skin cancer detection based on image processing, *Curr. Med. Imaging* 16 (2020) 50–58.
- [47] H. Zhou, G. Schaefer, A. Sadka, M.E. Celebi, Anisotropic mean shift based fuzzy c-means segmentation of dermoscopy images, *IEEE J. Sel. Top. Signal Process.* 3 (1) (2009) 26–34.
- [48] G. Zouridakis, M. Doshi, N. Mullani, Early diagnosis of skin cancer based on segmentation and measurement of vascularization and pigmentation in nevuscope images, *Engineering in Medicine and Biology Society* (2004).



Akemi Galvez works at Toho University (Funabashi, Japan) and the University of Cantabria (Santander, Spain), and is a member of the Computer Graphics and Artificial Intelligence (CGAI) research group. She has published more than 160 international papers in scientific journals and conferences, including papers in top journals of several categories of JCR, and holds three patents. She is also Editorial Board Member and reviewer of several JCR-indexed international journals. She has also been co-chair/co-organizer of prestigious international conferences such as ICMS'2006, ICCSA'2011, and Cyberworlds'2014, and reviewer/program committee member of several international conferences in the fields of computer graphics and artificial intelligence. Her research interests include geometric modelling and processing, shape reconstruction, artificial intelligence, soft computing, and their industrial applications.



Andres Iglesias works at Toho University (Funabashi, Japan) and the University of Cantabria (Santander, Spain), where he is Director of the Computer Graphics and Artificial Intelligence (CGAI) research group. He has published more than 250 scientific papers (including journal papers in 23 categories of JCR) and 14 books, and holds three patents. He is the current chair of IFIP TC5 WG5.10 and Editorial Board Member of 15 international journals. He has been chair/organizer of 55 international conferences and workshops and program committee member of more than 300 international conferences. He has been reviewer of about 200 international papers in journals (mostly in JCR journals) and more than 500 papers in international conferences, as well as expert evaluator of projects for NSF (USA), the European Commission (FP7 and Horizon 2020), and other national and regional public research agencies in several countries. His fields of interest are computer graphics, geometric modelling, artificial intelligence, and soft computing.



Iztok Fister received his degree in Computer Science from the University of Ljubljana, and his Ph.D. degree from the Faculty of Electrical Engineering and Computer Science, University of Maribor. Since 2010, he has been a Teaching Assistant with the Computer Architecture and Languages Laboratory, Faculty of Electrical Engineering and Computer Science, University of Maribor. His research interests include computer architectures, programming languages, operational researches, artificial intelligence, and evolutionary algorithms. In his research areas, he has published more original scientific papers, review papers, book chapters, edited books, and contributed to more than 50 international scientific conferences. He is also one of the presidents in the international student conference in computer science. In many journals with impact factor, he has been promoted as an outstanding reviewer.



Iztok Fister Jr. received his B.Sc., M.Sc. and Ph.D. in Computer Science from the University of Maribor, Slovenia. His areas of interest include data mining, pervasive computing, optimization and sport science. He has published more than 120 research articles in referred journals, conferences and book chapters. Furthermore, he is a member of the editorial boards of 5 different international journals, and he has acted as a program committee member in more than 30 international conferences. He is currently an assistant professor at the University of Maribor, Slovenia.



Cesar Otero received the degrees of B.S. (1983) and Ph.D. (1990) in civil engineering from the University of Cantabria (UC), Spain, where he is currently full professor. He introduced the line of studies of CAD (1989–1993) at the UC and founded the Research Group EgiCAD (Graphic Engineering and CAD) in 1999. He started to work in the field of BIM in 2005 and is currently the head of the Master BIM in UC. He has developed more than 60 R&D projects with several companies mainly with private funds. Mr. Otero received the international IASS Tsuboi Award in 2001 by his works in the design of Spatial Structures. He has received in 2016 the Outstanding Course Award (Open Education Consortium) by the subject “Workshop in Projects” into the Civil Engineering Degree in the School of Santander.



Jose A. Diaz received the M.C.E. from University of Cantabria, Major in Construction, Organization and Management, in 1998; and the Ph.D. in Civil Engineering, Major in Computational Geometry and Computer Aided Design from University of Cantabria, Spain, in 2008. He teaches graphic representation techniques in the Civil Engineering School of Cantabria. His main research interests include computational geometry and its application to the design of spatial structures, as well as the use of 2D Möbius Transformations in the modeling of three-dimensional shapes.